Materials Science & Engineering A 764 (2019) 138210

Contents lists available at ScienceDirect

Materials Science & Engineering A

journal homepage: www.elsevier.com/locate/msea

Damage mechanisms in selective laser melted AlSi10Mg under as built and different post-treatment conditions

Lv Zhao[a,b,*], Juan Guillermo Santos Macías[b], Lipeng Ding[b,c], Hosni Idrissi[b,c], Aude Simar[b]

[a] Department of Mechanics, Huazhong University of Science and Technology, Wuhan, China
[b] Institute of Mechanics, Materials and Civil Engineering, UCLouvain, Louvain-la-Neuve, Belgium
[c] EMAT, University of Antwerp, Antwerp, Belgium

ARTICLE INFO

Keywords:
Damage mechanism
Ductility
Selective laser melting
Heat treatment
Friction stir processing

ABSTRACT

Selective laser melting (SLM) manufactured AlSi10Mg alloys present a fine silicon-rich network and precipitates which grant high mechanical strength but low ductility. Post-treatments, aiming at eliminating inherent defects related to SLM such as residual stresses, porosity or inhomogeneity, result in significant changes in the microstructure and impact both the hardening and the damage mechanisms of the post-treated material. The present work is dedicated to the investigation of the fracture of SLM AlSi10Mg under as built and three post-treatment conditions, namely two stress relieve heat treatments and friction stir processing (FSP). It is found that the interconnected Si network fosters damage at low strain due to the brittleness of the Si phase. The onset of damage transfers load to the enclosed Al phase which then fractures quickly under high stress, thus leading to low material ductility. In contrast, when the Si network is globularized into Si particles, the ductility is highly increased even in the case where the porosity and inhomogeneity of the microstructure remain after the post-treatment. The ductility enhancement results from the delay in void nucleation on the Si particles as well as from the tolerance for void growth in the Al matrix.

1. Introduction

Additive manufacturing (AM) of metal parts is getting intensive attention as it significantly relieves the constraints on structural design and optimization present in traditional manufacturing methods. The flexibility and material saving features related to the AM technology promote its applications in aerospace, automotive and biomedical industries [1,2].

Among AM metallic materials, selective laser melted (SLM) AlSi10Mg [3] offers good balance between weight and strength and thus is the subject of an increasing number of investigations. However, SLM AlSi10Mg also presents shortcomings which cannot be eliminated just through building parameter optimization [4]. Inherent defects of SLM, such as porosity [5], microstructural inhomogeneity (melt pool structure) [6,7] and residual stresses, compromise the performance of this Al alloy, which generally presents low ductility and poor fatigue resistance [8,9].

In order to improve the mechanical properties of SLM AlSi10Mg, a variety of post-treatments, mostly based on heat treatment, have been developed. Both annealing at relatively low temperature (typically 300 °C) [10] and solution treatment at relatively high temperature (500 °C) [10–12] were applied, which resulted in globularization of the continuous Si network and residual stress relief, thus improving ductility and fatigue resistance. The high temperature heat treatments have furthermore potential to homogenize the microstructure, but they generally led to very significant strength loss due to microstructure coarsening [10,12], which could not be compensated by precipitation via aging due to the limited Mg content [10]. Thermomechanical treatments such as hot isostatic pressing (HIP) [13,14] and friction stir processing (FSP) [15–17] were also employed to ductilize SLM AlSi10Mg. These two treatments offer the possiblity of reducing porosity, which cannot be achieved by heat treatment, as reported in studies on SLM Ti6Al4V alloy [18,19] and SLM AlSi10Mg [5,16]. While FSP has shown very significant porosity reduction and fatigue life improvement by a factor higher than 100 [16], HIP has not yielded satisfactory results for SLM AlSi10Mg due to coarsened microstructure [13,14] and moderate porosity reduction capacity [5].

Thermal or thermomechanical post-treatments on SLM AlSi10Mg invariably alter the microstructure, mostly leading to a change in the Si-rich phase. In this context, it must be noted that both strength and damage are strongly related to this hard phase in SLM AlSi10Mg. The continuous Si-rich network has been shown to exhibit strong load

* Corresponding author. Institute of Mechanics, Materials and Civil Engineering, UCLouvain, Louvain-la-Neuve, Belgium
E-mail addresses: lv.zhao@uclouvain.be, lvzhao@hust.edu.cn (L. Zhao).

https://doi.org/10.1016/j.msea.2019.138210
Received 26 May 2019; Received in revised form 23 July 2019; Accepted 24 July 2019
Available online 27 July 2019

bearing effect [20,21]. This can be analogous to fiber reinforced composites [22]. Moreover, it was proposed that the Si network can efficiently limit the dislocation movement during deformation [9,23], thus resulting in significant hardening. The grain size of the Al phase is expected to have minor effect on the strength, since SLM AlSi10Mg generally presents much larger grain size than that of the Si-rich network or Si particles [9,23,24]. Damage behavior is also controlled by the Si-rich phase, as strain incompatibility and localization occur at the Al/Si interface, and the Si phase is subject to higher stress [20]. The AlSi10Mg can be considered as an Al matrix which incorporates a hard secondary phase in the form of either a network or globules. According to expertise in the fracture community, mostly acquired through particulate damage sources, damage behavior is highly dependent on the strength, shape, size and distribution of the secondary phase [25,26]. It has been recently shown that higher ductility can be reached with smaller size and more homogeneous distribution of the secondary phase particles [27]. Although ductilization of AM AlSi10Mg by post-treatments has been widely reported [10,12,14], the fundamental mechanism has been rarely addressed [20] and the factor dictating ductility remains unravelled.

This work focuses on the study of damage behavior of SLM AlSi10Mg. Four different states are considered, involving different thermal and thermomechanical post-treatments and thus different microstructures, strength and ductility. The four microstructures studied here cover the gradual evolution of the Si-rich phase from interconnected network state (as built) to totally globularized state with and without (i.e. FSP case) initial porosity. The aim is to investigate the damage behavior in different microstructural states and to correlate it with the ductility. In addition to the as built state, the three other microstructures are obtained via two heat treatments and friction stir processing. The ductility of the material, denoted by the macroscopic fracture strain, is obtained from uniaxial tensile tests. The damage mechanism is addressed with notched tensile samples with total and partial failure stages. Finite element simulations are employed to couple the local strain field to the damage characteristics revealed through the experiments.

2. Experiments

2.1. Material and post-treatment conditions

AlSi10Mg plates of 150 × 35 × 5 mm were manufactured using an EOS M290 machine with a build platform temperature of 35 °C. The machine manufacturer optimized parameters were set as follows: laser power of 390 W, layer thickness of 30 μm, hatch spacing of 0.19 mm, scan speed of 1300 mm/s and scan rotation of 67°. The chemical composition of the SLM AlSi10Mg alloy was measured by the inductively coupled plasma optical emission spectroscopy (ICP-OES) technique, see Table 1. After manufacturing, three different post-treatments were performed on the as built (AB) plates. The four studied states are presented in Table 2.

The first two post-treatments involved a residual stress relieve heat treatment performed under Ar atmosphere (SRHT). SRHT1 denotes a heat treatment at 250 °C for 2 h while SRHT2 denotes a heat treatment at 300 °C for 2 h. The third post-treatment was friction stir processing (FSP). FSP, derived from friction stir welding [28,29], allows reducing porosity and breaking down and homogenizing secondary phase particles [27]. FSP was conducted on a Hermle UWF 1001 H milling machine, using a tool made of H13 steel. The backing plate and the clamping system were installed in a tank containing cutting oil to increase the cooling rate. The FSP tool is composed of a scrolled shoulder of 20 mm in diameter and a pin of 4.6 mm in length. The pin is threaded and presents three flats corresponding to three sides of a hexagon inscribed in the circle of the pin (see Ref. [30] for a schematic view of the tool geometry). During FSP, the tool penetrated the AlSi10Mg plate with a plunge depth of 4.7 mm and stirred the material with a rotational speed of 1000 rpm and a traverse speed of 500 mm/min. In order to preserve the fine Si-rich phase, only 1 FSP pass was performed.

Table 1
Chemical composition in % wt. of the SLM AlSi10Mg.

Al	Si	Mg	Fe	Na
Bal.	9.68	0.40	0.13	0.02

Table 2
Different states of SLM AlSi10Mg studied in the present work.

Designation	Condition
AB	SLM as built
SRHT1	AB + Heat treatment at 250 °C for 2 h
SRHT2	AB + Heat treatment at 300 °C for 2 h
FSP	AB + Friction stir processing (1 pass)

2.2. Characterization

2.2.1. Microstructure characterization

The microstructures of the four different states were visualized using scanning electron microscopy (SEM, ZEISS FEGSEM ultra 55). The SEM samples were first polished to mirror-like surface and then etched with an HF (0.5 vol%) solution to reveal the Si-rich phase. The microstructural analysis was performed with the ImageJ software.

Both the Si-rich and the Al phases in the four states were further analyzed with a FEI Osiris Transmission Electron Microscope (TEM) equipped with a CHEMISTEM detector. The TEM samples were prepared using a dual-beam focused ion beam (FIB) instrument (FEI Helios Nanolab 650). The FIB extraction was performed in the center of the melt pool or in the center of the FSP stir zone.

2.2.2. Mechanical testing

Uniaxial tensile tests were performed following ASTM E8/E8M-15a standard. Horizontally oriented (with regard to the SLM building platform) round tensile test specimens were extracted by machining from the AB plates and from the FSP zone (see Fig. 1). SRHT1 and SRHT2 specimens were heat treated in Ar environment after machining.

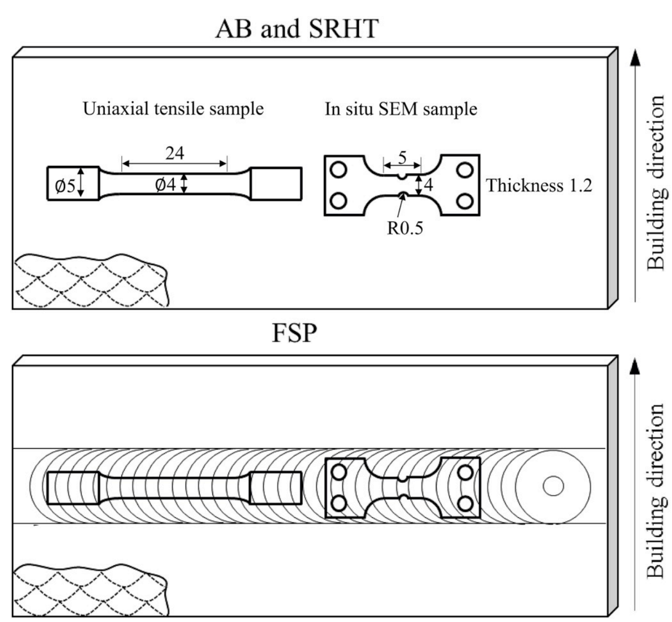

Fig. 1. Geometry and extraction position of mechanical test samples. The loading direction is perpendicular to the building direction in the present work.

The tests were carried out with a Zwick tensile machine, using a loading rate of 1 mm/min.

In order to investigate the damage mechanisms, in situ SEM tensile testing was conducted on notched specimens (see Fig. 1) to monitor the correlation between the damage and the microstructure. Both surfaces of the specimens were polished, with one side polished to 1 μm and finished with oxide polishing suspension (OPS) and chemically etched. The tests were performed with a Gatan microtest tensile stage using a loading rate of 0.1 mm/min. After fracture, the samples were polished to mid-thickness for an in-depth study of fine local damage.

To minimize the influence of the heat affected zone (HAZ) at the melt pool border which does not exist in the FSP state [16], and to study the most representative microstructure, i.e. the fine melt pool zone, all the mechanical tests were performed in the horizontal direction, which is perpendicular to the SLM building direction (see Fig. 1).

3. Finite element modeling

Finite element simulations were performed with Abaqus 2016 [31] to assess the local strain prior to dense damage in the notched samples during the in situ SEM tensile tests. The simulations incorporated the real sample geometry and the material properties for each microstructural state. Fig. 2 depicts the model geometry, the boundary conditions and the mesh. To simulate the in situ tensile testing, the left side of the part was fixed, and the right side was subjected to a displacement. The central region of the model was meshed with C3D8 elements presenting a size of about 50 μm, and the rest with C3D6 elements with gradual size from 50 μm to 0.6 mm. The part was meshed with 20 layers of elements in the thickness to capture the large strain gradient. It should be noted that the present model considered only the macroscopic plastic behavior of the material, damage or crack propagation were not included since only the very early stage of damage confined in the notch region was investigated during the in situ SEM tensile tests.

4. Results

4.1. Microstructure

The representative microstructures of the four AlSi10Mg states are

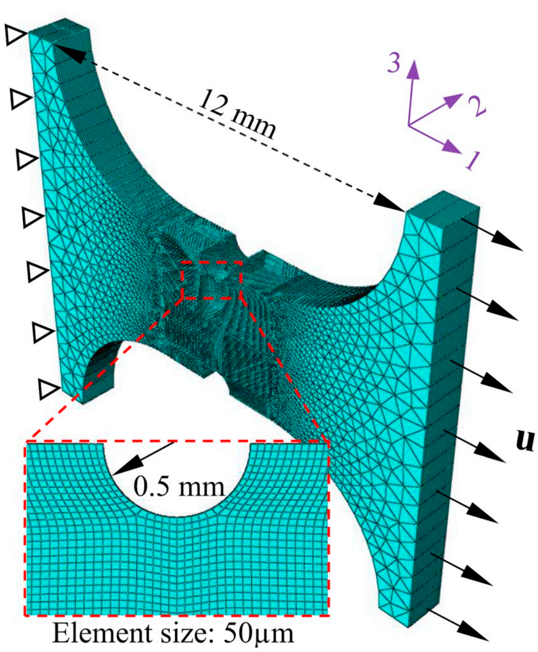

Fig. 2. Finite element model incorporating the geometry of the in situ SEM tensile sample.

presented in Fig. 3. The heterogeneity in the microstructure, in particular the HAZ, is not in the scope of the present study since it is not of first order importance in the damage behavior for the loading direction applied in this work (see Fig. 1), as will be shown in section 4.3.3. Figs. 4 and 5 present a quantitative analysis of the particle objects observed in Fig. 3. The AB state presents a thin Si-rich network, which is mostly interconnected and encloses the α-Al matrix (Fig. 3a). The Al cells contain very fine precipitates of a diameter generally smaller than 20 nm, as presented in the inset of Fig. 3a as well as in Fig. 4a and c. Fig. 3b shows that the Si network and the embedded precipitates are preserved in the SRHT1 material. However, the Si network becomes thicker than in the AB state, as can be noticed in the inset of Fig. 3b. Moreover, the precipitates inside the Al cells become larger (see Fig. 4c) and present an acicular shape, as evidenced in Fig. 4b and quantified by the aspect ratios (Fig. 4d). The precipitates in the AB and SRHT1 states present a surface area fraction generally above 2%. Their nature will be addressed in the TEM results.

When the heat treatment temperature is higher, as in the case of SRHT2, the Si network is totally broken down and transformed into Si-rich particles (see Fig. 3c). The microstructure is inverted, i.e., the Si-rich particles are surrounded by the α-Al phase. These particles have a wide size range. The small ones have a diameter lower than 50 nm and the big ones can reach hundreds of nanometers (inset of Fig. 3c). The large size variation is likely due to the fact that the big particles are globularized from the initial Si-rich network and the small ones grow up from the initial fine precipitates, as reflected by the bimodal size distribution presented in the inset of Fig. 5c, evidenced by the two red arrows. Regarding the microstructure of the FSP state (Fig. 3d), the globularized Si-rich particles are dominant, similarly to the SRHT2 state. However, the Si-rich particles are larger (Fig. 5c) and thus involve a greater inter-particle distance (Fig. 5d) compared to the SRHT2 microstructure. It is worth mentioning that the nearest neighbor distance analysis excluded 30% in volume of the smallest particles to acquire a more representative particle spacing. The threshold of 30% is considered here to remove the smaller population of the Si-rich particles in the SRHT2 state.

Fig. 6 shows TEM micrographs of the four states reported in Table 2. The STEM-EDX analysis shows that the fine precipitates inside Al cells of the AB and SRHT1 states are Si-rich precipitates (see insets of Fig. 6a and b). There is a lack of concentrated points in the corresponding Mg maps (not presented here) at the same location as the insets of Fig. 6a and b, suggesting that these precipitates are not Mg_2Si as one could have suspected. In the SRHT2 sample, Fig. 6c clearly shows the two populations of Si particles, as captured in the size distribution analysis (see inset of Fig. 5c). It is also revealed that the Si particles are very close to each other and several are overlapped through the TEM sample thickness. Some acicular particles can still be observed in the SRHT2 microstructure (yellow arrow in Fig. 6c). In the FSP state, the small particles are no longer present (Fig. 6d); this is likely due to the solutionizing effect of the relatively high temperature (500 °C [16]) reached during FSP. The evolution of the chemical composition of the Al matrix phase is revealed by the STEM-EDX analysis (Fig. 6e). In the AB state, the Al phase contains 2.2 at.% of Si in solution, which implies that the Si was supersaturated in the Al matrix during the rapid cooling in the SLM process, as already discussed in literature [12]. The saturated Si then precipitated during all three post-treatments, as evidenced by the very low Si content in the Al matrix (Fig. 6e).

According to our former work [16], the AB state involves an initial porosity of 0.09% (volume fraction of porosity larger than 5 μm equivalent diameter). The porosity level for the SRHT state is similar [16]. Nevertheless, the porosity in the FSP state is strongly reduced to 0.02% thanks to the thermomechanical effect of FSP. Moreover, FSP eliminates the melt pool structure [16] which is however present in AB, SRHT1 and SRHT2 states (see Supplementary Fig. 1).

The aforementioned four model microstructures are ideal for analyzing the influence of various features on damage. For instance, we can

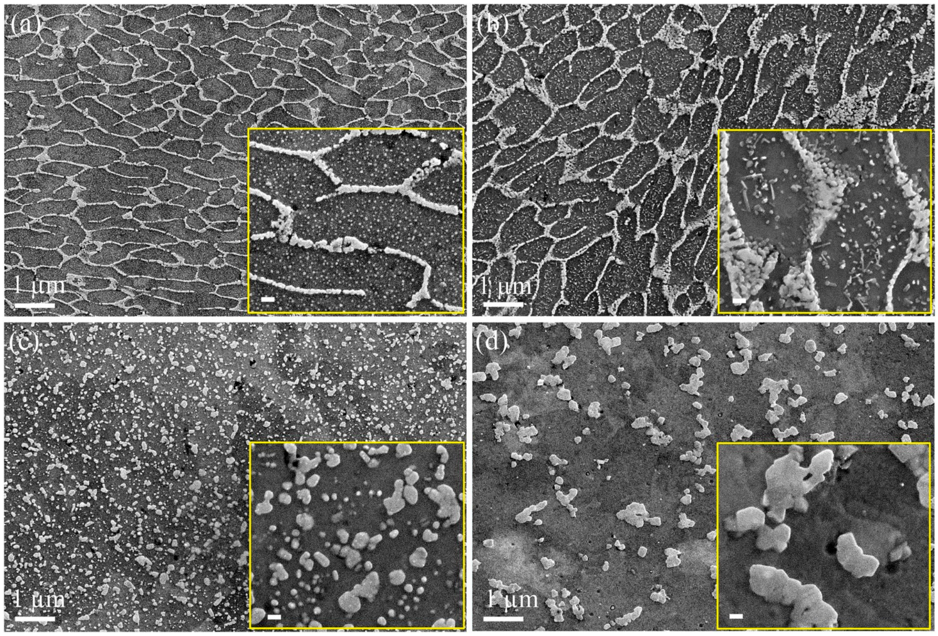

Fig. 3. Microstructure of SLM AlSi10 Mg at the following states: AB (a), SRHT1 (b), SRHT2 (c), and FSP (d). The scale bars in the insets represent 100 nm.

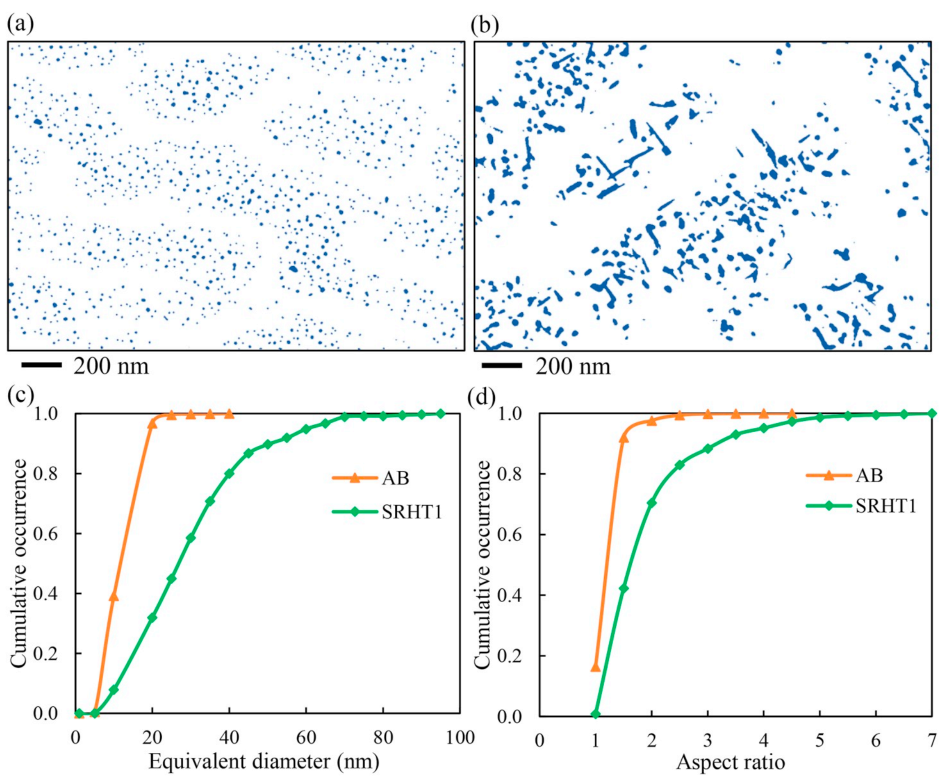

Fig. 4. Fine precipitates in both AB (a) and SRHT1 (b) states and their equivalent diameter (c) and aspect ratio (d) distributions.

treat the form of the Si phase (AB versus SRHT2), the size of the Si network and Si precipitate (AB versus SRHT1), the initial porosity (AB versus SRHT2 and SRHT2 versus FSP) and the size of the Si particles (SRHT2 and FSP).

4.2. Tensile properties

The tensile properties are summarized in Table 3 and also presented by the curves relating true stress and true strain till fracture in Fig. 7. The dashed lines in Fig. 7 represent the stress-strain relationship after necking obtained using a Hollomon law fitting (see Supplementary Table 1). Note that the stress at fracture point predicted with the fitted Hollomon law presents only a difference of 5% compared to the stress calculated with final external load and cross section area. The strain at fracture is calculated using Eq. (1) with the initial (A_0) and final (A_f) section areas measured with a profile projector.

$$\varepsilon_f = ln\left(\frac{A_0}{A_f}\right) \tag{1}$$

The AB state presents the highest mechanical strength but the

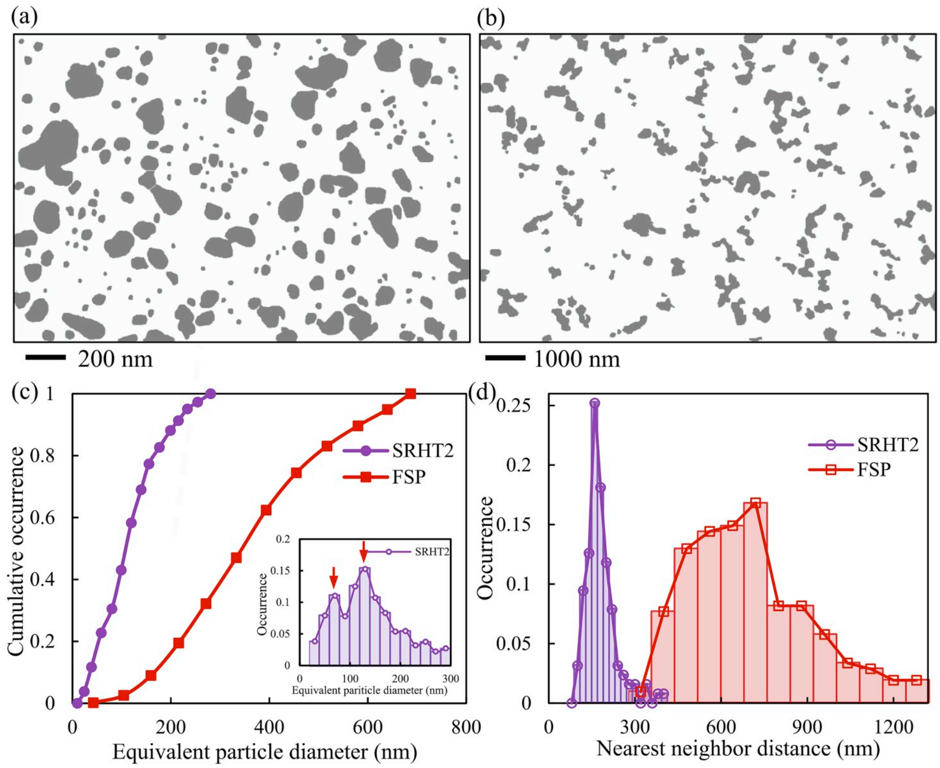

Fig. 5. Si-rich particles in both SRHT2 (a) and FSP (b) states and their area-weighted size (c) and nearest neighbor distance (d) distributions. The distribution analysis incorporates about 500 particles for both states. The lines in (c) and (d) are plotted from the center points of the histogram bins. The inset in (c) highlights the bimodal distribution of the SRHT2 Si-rich particles which is also evidenced by the two red arrows. (For interpretation of the references to colour in this figure legend, the reader is referred to the Web version of this article.)

lowest ductility. The high strength could be related to the load bearing of the Si network as well as the barrier effect of the Si phase, i.e. both network and fine precipitates (Figs. 3a and 6a), against the dislocation movement [9, 23]. Indeed, recent works involving in situ neutron diffraction tensile tests reported the stress reached in the Si network to be more than twice that in the Al phase [20,21]. The SRHT1 state presents lower mechanical strength than the AB state but very similar ductility. The decrease in strength is expected to be the result of precipitate coarsening inside the Al cells (Figs. 3 b and 6 b), which reduces the hardening capacity. Regarding the SRHT2 and FSP states, where the Si network has been globularized, the ductility becomes significantly higher than that of the AB and SRHT1 states, by a factor of 4 (see Table 3 and Fig. 7). The increase in ductility is however accompanied by a strength loss. The main reason for the strength decrease in the SRHT2 and FSP samples is that the load bearing effect of the globular shape (Si particle) is lower compared to that of the elongated shape (Si network) reinforcement, as predicted by the shear lag theory [32]. The growth or suppression of fine precipitates leads to further strength loss. Nevertheless, the SRHT2 and FSP states involve very similar mechanical strength and ductility. This provides two ideal microstructures for investigating the size effect of the Si phase on damage behavior.

4.3. Damage

4.3.1. In situ tensile testing

In situ SEM tensile tests and subsequent characterization were conducted to investigate the damage mechanism and its link with the microstructure. These tests were also coupled with finite element simulations which allowed assessing local strain in the damaged region. The loading was interrupted to observe the deformed microstructure and to record the notch extension at different force levels, which served to validate the finite element modeling, as will be presented later in this section.

The final fractured status are presented in Fig. 8. It can be noticed that the heat affected zone (HAZ), as indicated by the yellow dashed arrows in Fig. 8a–c, is not in favorable orientation to participate to crack initiation and propagation (refer to Fig. 1) despite slight strain localization and occasional fracture path reorientation (blue arrow in Fig. 8a). Some microcracks traversing the melt pools are found in the SRHT samples (green arrows in Fig. 8b and c). In the FSP state the HAZ is completely removed in the stir zone due to the microstructure homogenization.

The recorded in situ tensile data were used to validate the finite element model. Four simulations were performed, incorporating the material properties (plastic behaviors) of the four states obtained from the uniaxial tensile tests (Fig. 7). The simulations are compared with the in situ tensile tests in terms of load-notch extension prior to cracking, as presented in Fig. 9. Here the notch extension denotes the difference between the current and the initial notch widths. This gives a more accurate indication than the global extension which involves the deformation of the whole tensile set-up.

It is found that the simulations are in good agreement with the real experiments, which gives confidence for using the simulation to evaluate the macroscopic strain in the notch region of the sample prior to unstable fracture. It should be noted that the macroscopic strain for damage or fracture assessment is a more appropriate indicator for engineering applications than the microscopic strain at very fine scale, such as the scale of Si particles or Al grains. The latter is more important for micromechanics modeling of fracture, which is however not in the scope of the present work. Fig. 10 depicts the damage status as a function of plastic strain in both the SRHT2 and FSP samples. No damage was captured in the AB and SRHT1 samples before the final fracture occurred. The void nucleation proportion in Fig. 10e was calculated with the number of damaged particles (both particle fracture and decohesion) and the number of particles excluding the smallest ones that present a volume fraction of 30%, similarly to the particle spacing analysis already discussed in section 4.1 in relation to Fig. 5d. It can be noticed that the damage appears much later (at an estimated strain of 0.24) in the SRHT2 sample compared to the FSP one (at an estimated strain of 0.09). However, the nucleation rate with increased strain level seems to be similar in both states (Fig. 10e). This is probably due to the similar flow stress at identical strain between the SRHT2 and

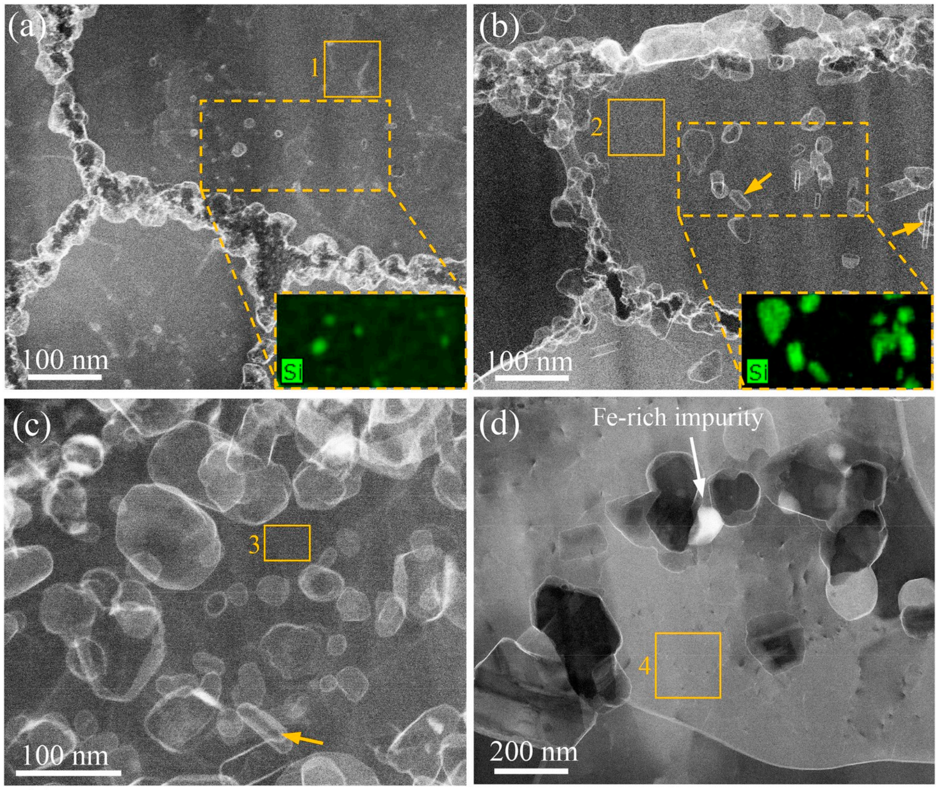

(e)

Material	Zone	Al (at.%)	Si (at.%)	Mg (at.%)
AB	1	97	2.2	0.7
SRHT1	2	98.9	0.2	0.8
SRHT2	3	99.2	0.2	0.6
FSP	4	98	0.3	1.7

Fig. 6. HAADF-STEM images and STEM-EDX analysis of the four microstructures. AB with local Si map as inset (a), SRHT1 with local Si map as inset (b), SRHT2 (c), FSP (d), and the STEM-EDX analysis of α-Al composition performed in the numbered rectangular regions (without Si precipitates) in (a)–(d) (e). The insets in (a) and (b) share the scale bars with (a) and (b), respectively. The arrows in (b) and (c) point out the acicular Si particles.

Table 3
Tensile properties of the four states of SLM AlSi10Mg. Mean values and standard deviations are obtained from at least three samples for each state. The reported values are true strain and true stress.

Designation	Yield strength (MPa)	Stress at necking (MPa)	Strain at necking	Strain at fracture
AB	287 ± 2	525 ± 4	0.11 ± 0.006	0.11 ± 0.006
SRHT1	249 ± 2	421 ± 2	0.07 ± 0.001	0.12 ± 0.01
SRHT2	212 ± 12	341 ± 16	0.06 ± 0.003	0.42 ± 0.06
FSP	189 ± 5	357 ± 11	0.12 ± 0.004	0.40 ± 0.06

FSP samples (Fig. 7). Although the void nucleation rate is assessed with the surface observations which are not fully representative, it should be noted that the main message brought about by these observations is clear and trustworthy, i.e., damage nucleation occurs later in the SRHT2 sample compared to the FSP sample.

4.3.2. Fracture surface morphology

The fracture surfaces of the in situ tensile specimens were observed under SEM, as presented in Fig. 11. The crack initiation sites are located at the mid-thickness plane of the notch, where the stress triaxiality is the highest (see Supplementary Fig. 2). The AB and SRHT1 samples present lamellar features (see Fig. 11a and c), which reflect well the Si

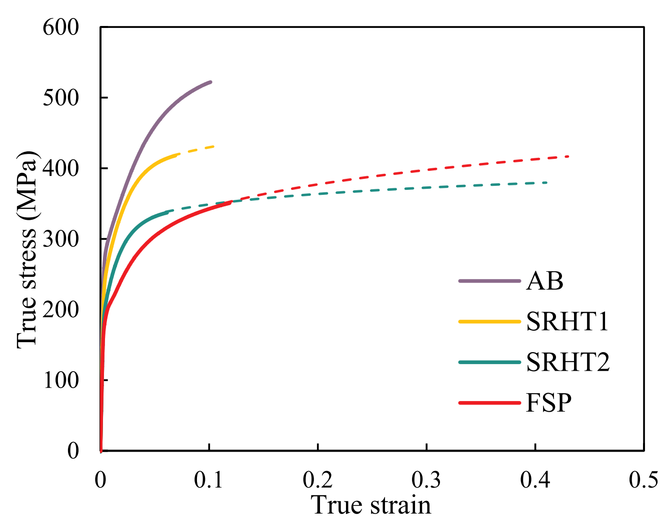

Fig. 7. True stress-strain curves derived from uniaxial tensile tests. The dashed lines represent the post-necking behaviors fitted with a Hollomon law.

network (see Fig. 3a and b). Regarding the SRHT2 and FSP samples, the fracture surfaces present dimples as typically found in ductile materials (Fig. 11e and g). The dimple features indicate that the fracture is driven by void nucleation, growth and coalescence [33]. Moreover, the

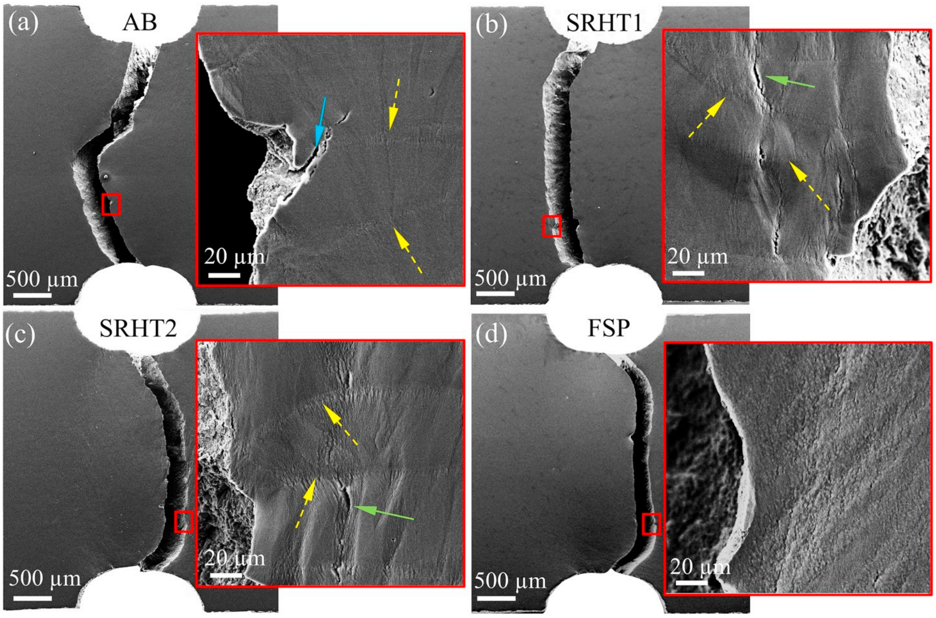

Fig. 8. In situ tensile testing of SLM AlSi10 Mg at the following states: AB (a), SRHT1 (b), SRHT2 (c), and FSP (d). The zooms are taken from the regions inside the red boxes. The blue arrow in (a) highlights that the HAZ may occasionally reorient the crack during propagation. The yellow dashed arrows in (b) and (c) indicate deformed HAZ at the melt pool border and the green arrows highlight microcracks traversing the melt pool. (For interpretation of the references to colour in this figure legend, the reader is referred to the Web version of this article.)

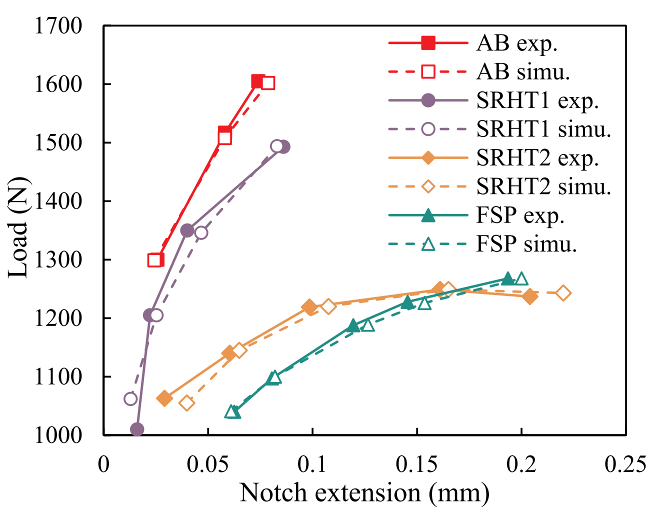

Fig. 9. Validation of finite element simulations with the notch extension-load relationship of the in situ tests.

dimples are smaller in the SRHT2 sample, which correlates with the smaller Si particles, compared to the FSP sample, considering that both samples have similar fracture strain (see Table 3).

The detailed morphologies (Fig. 11b, d, f, and h) are examined at higher magnification (× 50 k). Some parts of the Si network are observed near the border of the lamellar features in the AB and SRHT1 samples, as indicated by the arrows in Fig. 11b and d. At this stage, it is still not clear whether damage nucleates along the Si network by decohesion or if the crack propagates along the network. In particular, extremely fine dimples are observed on the Al phase of the AB sample (see inset of Fig. 11b). They are likely generated by the fine precipitates inside the α-Al illustrated in Fig. 3a. Regarding the two gobularized states, some Si particles are found inside the dimples (Fig. 11f and h). Moreover, fractured particles are frequently present in the dimples of the FSP sample.

4.3.3. *Damage features*

The fracture surface observation alone does not allow a full understanding of damage nucleation. Therefore, the fractured samples were polished to the mid-thickness plane to visualize the local damage and its correlation with the Si-rich phase (Fig. 12). A large magnification (× 50 k) is used to clearly reveal the local damage, which is generally smaller than 1 μm. The damage is related to the Si phase in all the studied states. In the cases of AB and SRHT1 the damage mostly nucleates from the breakage of the Si network (Fig. 12a–b); interface decohesion can be occasionally observed at local discontinuous network ends or network junctions. Some cracks can be observed in the Al cells enclosed by the network (Fig. 12c and d). The fine precipitates can very locally change the fracture surface roughness and leave extremely small dimples, as observed in Fig. 11b. In the SRHT2 and FSP samples, the damage nucleates on the Si particles by both particle fracture and particle-matrix decohesion (Fig. 12e and f). According to statistics performed on a reasonably large number of damaged particles (500 for the SRHT2 sample and 250 for the FSP sample), particle fracture represents 4% of the damage nucleation sites in the SRHT2 state and 25% in the FSP state. Moreover, it can be seen that the voids are very close in the SRHT2 state, which favors fast coalescence after nucleation, as highlighted by the dashed circle in Fig. 12e.

It is worth mentioning that the HAZ barely contributes to damage when loading is perpendicular to the building direction, although the melt pool border region undergoes slight strain localization (see Fig. 8a–c). As shown in Fig. 13 for the AB condition, most of the Si-rich phase is intact in the HAZ (region 1), while dense voids, generated from the interconnected Si-rich network, are observed in the melt pool interior just nearby the HAZ (region 2). The HAZ might play a more important role in damage if loading is parallel to the building direction due to its lower strength, as recently reported [7]. The present work is focused on samples loaded horizontally with respect to the building direction where damage is observed in regions that correspond to most of the volume of the sample. Note also that the HAZ has been completely suppressed in the FSP sample (Fig. 8d.). It is thus pertinent to minimize its effect in the other states for comparison.

4.3.4. *Damage statistics*

The damage mechanisms have been identified in the previous section. This section is devoted to investigating damage size and distribution upon fracture propagation. According to the uniaxial tensile tests, similar ductility is found for AB and SRHT1 samples on the one side, and for SRHT2 and FSP samples on the other side (Table 3). In order to further correlate ductility with microstructure, damage statistics are performed at the mid-thickness plane in the notch region close to the fracture surface (Fig. 14), where the local strain can be

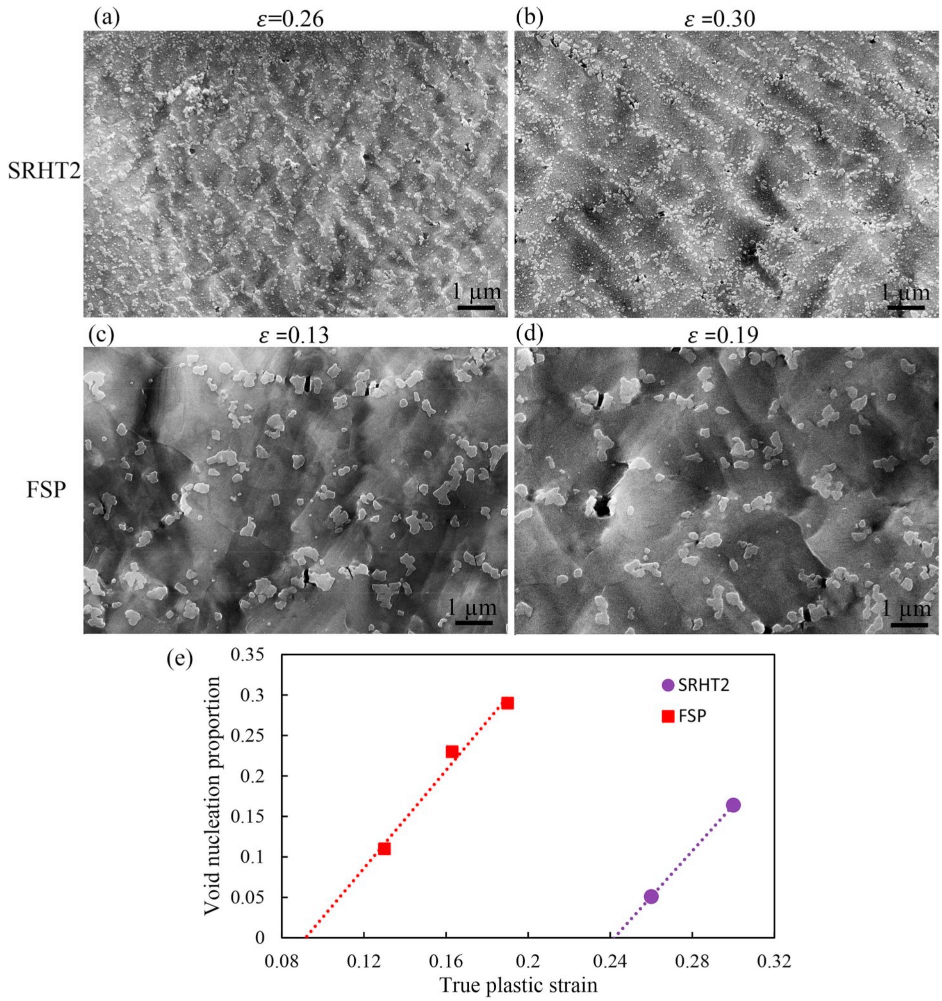

Fig. 10. Damage observation during the in situ tensile tests. Damage nucleation at a strain of 0.26 (a) and of 0.30 (b) in the SRHT2 state, damage nucleation at a strain of 0.13 (c) and of 0.19 (d) in the FSP state, the evolution of void nucleation proportion as a function of true plastic strain (e). The local strain values are extracted from finite element simulations of the notched samples.

considered close to the true fracture strain.

The damage (equivalent diameter) size distribution and the damage density are investigated based on the voids included in the notch region (Fig. 14). Interestingly, it is found that the SRHT2 state involves very similar damage size distribution to that of the AB state (Fig. 15a). In addition, the damage size in both samples is the smallest. The void size in the SRHT1 sample is larger than the AB, which is due to coarsened microstructure (Figs. 3 and 4), as can be clearly seen in Fig. 14. The FSP sample involves the largest damage size (Fig. 15a), which can be explained by the fact that the damage nucleates relatively early (at an estimated strain of 0.09), so it significantly grows and eventually coalesces with its neighbor (indicated by the arrow in Fig. 14d) before the final failure at a strain of 0.4.

When plotting the damage density (void number/area) versus the surface area fraction of the damage for the four microstructures (Fig. 15b), it is revealed that the AB state involves lower damage density than the SRHT2 state while they have similar damage size (Fig. 15a). This implies that the coalescence takes place shortly after damage nucleation in the presence of the Si-rich network, which cuts down further nucleation events. When comparing the states with close ductility, it is found that the AB and SRHT1 present similar behavior. The damage is slightly denser but smaller in the AB state. The larger surface area fraction of damage in the SRHT2 sample can be related to the softer Al matrix (larger precipitates, see Fig. 4) which allows more void growth. However, the damage behavior significantly differs between the SRHT2 and FSP samples. The void number is much higher in the SRHT2 state, but as the individual void size is much smaller, the total damage area is lower than the FSP state. This indicates that the ductilization is achieved differently by the heat treatment and the FSP performed in the present work, as will be discussed in the following section.

5. Discussion

5.1. Damage mechanism

A damage mechanism for the four microstructures is proposed (Fig. 16) based on the observations in sections 4.3.2-4.3.4. When the Si network is present (AB and SRHT1), excessive damage nucleates on the network at a low strain (< 0.1), since the Si phase is mostly interconnected and cannot bear high strain before failure. As mentioned in section 4.2, the high strength in the AB and SRHT1 samples is due to the load bearing capacity of the Si network. Once damage initiates, the Si network will simultaneously transfer the load to the enclosed Al phase as well as the part of the network without damage, which fracture quickly and connect the voids (see Fig. 12c–d). This mechanism explains the presence of lamellar features and segments of Si network on the fracture surface (Fig. 11b and d). It is worth noting that the aforementioned damage mechanism is different from the void-sheet scenario [34] which involves a coalescence of voids wide apart through

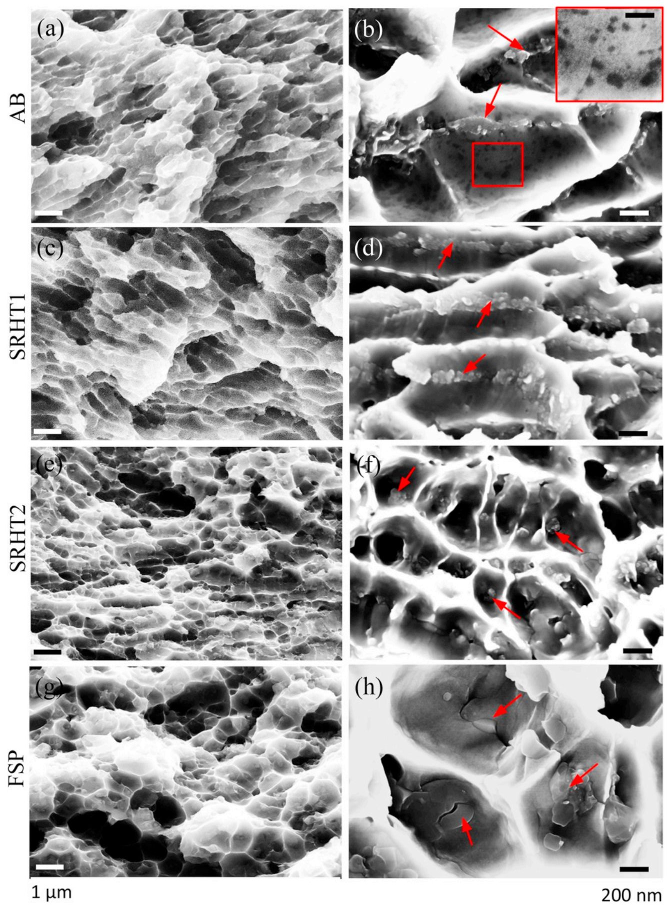

Fig. 11. Fracture surface morphology of SLM AlSi10 Mg at the following states: AB (a) and (b), SRHT1 (c) and (d), SRHT2 (e) and (f), and FSP (g) and (h). The arrows in (b) and (d) indicate the Si network, while those in (f) and (h) point to Si particles. The inset in (b) shows the rectangular area, incorporating a scale bar of 100 nm.

shear bands.

In the two cases of globularized microstructure (SRHT2 and FSP), the damage nucleates at lower macroscopic strain (see Fig. 10) in the FSP state since the Si particles are larger compared to the SRHT2 state (see Fig. 5c). Indeed, the particle fracture stress or particle/matrix decohesion stress is highly dependent on size; a smaller particle contains statistically less internal defects and thus presents higher failure stress [35]. The particle size effect on damage nucleation has also been reported in the case of wrought Al 6xxx alloys in which the damage nucleates on Fe-rich intermetallic particles [26,27]. Though damage appears earlier in the FSP sample, the particle spacing is much larger (Fig. 5) and there is more room for void growth before coalescence. On the other hand, damage nucleates late in the SRHT2 sample but the void coalescence takes place quickly due to the small inter-particle spacing. As a result, a similar ductility is reached in the two globularized microstructures through different void nucleation, growth and coalescence kinematics.

5.2. Ductilization route

Ductilization is generally achieved at the expense of mechanical strength. However, the gain will be limited if the damage origin remains unchanged [26]. The SRHT1 state retains the network and presents similar ductility as the AB state, while the SRHT2 and FSP states incorporate Si particles and exhibit a fourfold ductility increase. As the low ductility of the as built SLM AlSi10Mg alloy is controlled by the Si-rich network, globularization of the Si phase is critical to enhance

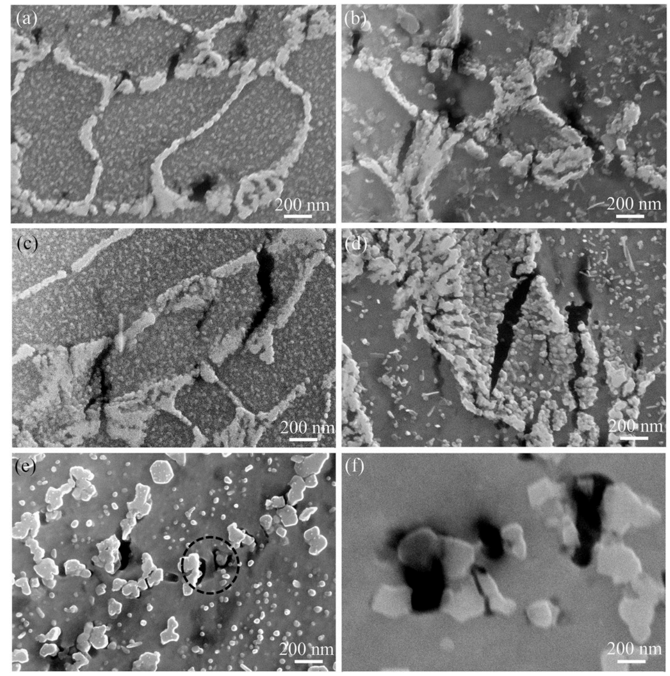

Fig. 12. Identification of damage sources. Si network breakage in the AB (a) and SRHT1 (b) states, nano-size cracks crossing the Al cell in the AB (c) and SRHT1 (d) states. Si particle fracture and Si/Al decohesion in the SRHT2 (e) and the FSP (f) states. The dashed circle in (e) highlights an ongoing coalescence between two voids. The loading is in the horizontal direction.

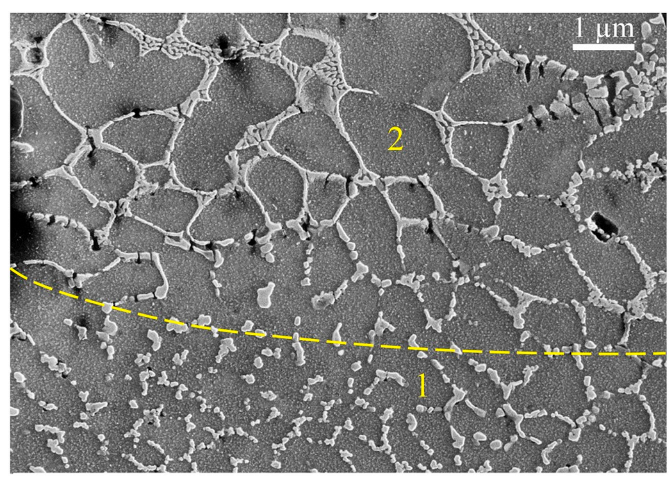

Fig. 13. Damage state in the HAZ and the melt pool interior of the AB sample. The region 1 highlights the HAZ where little damage can be observed, the region 2 highlights the part of the melt pool close to the HAZ where dense damage is present. The loading is in the horizontal direction.

ductility.

Through the comparisons between the SRHT1 and SRHT2 samples, i.e. similar porosity but different microstructures, as well as between the SRHT2 and FSP samples, i.e. different porosities but similar microstructure, it can be concluded that the porosity has negligible effect on the ductility of the four states investigated in the present work. This further confirms that the low ductility in the AB and SRHT1 states is driven by the Si-rich network rather than by initial pores. It should also be pointed out that porosity will impact ductility when it is sufficiently large, as investigated in Ref. [36] where the authors have introduced intentional penny shape pores and shown that only a pore larger than 450 μm can reduce the ductility of a cylindrical sample with a gauge diameter of 6 mm. However, in the present work, the porosity in the AB

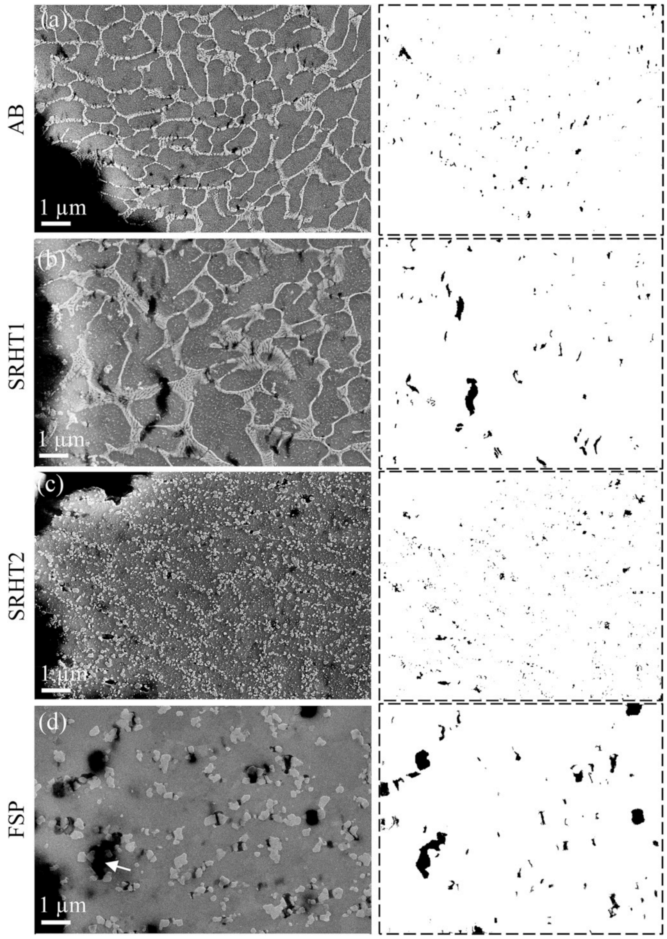

Fig. 14. Damage in SLM AlSi10 Mg at the following states: AB (a), SRHT1 (b), SRHT2 (c), and FSP (d). On the left, SEM images. On the right, image thresholding for the identification of damage. The arrow in (d) indicates a coalescence event. The loading is in the horizontal direction.

material is 0.09%, with pore equivalent diameter generally smaller than 50 μm, as revealed in our previous work [16]. The impact of relatively low initial porosity on ductility has been discussed in a recent work dealing with a cellular automaton micromechanics based damage model [26], where the authors showed that the initial porosity (0.12%) has limited effect in the hard Al matrices of 6xxx alloys in T4 and T6

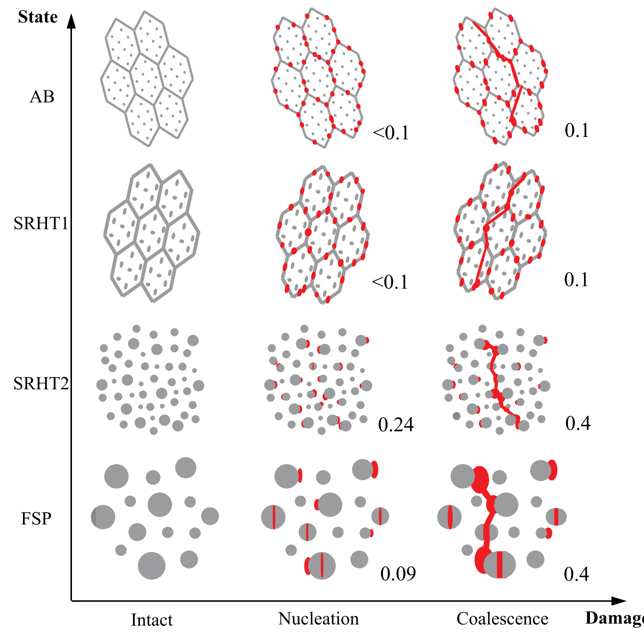

Fig. 16. Schematic drawing of the damage development in the four considered states of the SLM AlSi10Mg alloy. The strain at which the phenomenon is observed is indicated next to the relevant microstructure schematic.

states. These alloys present a similar yield strength to the AB and SRHT states investigated in the present work.

Heat treatment at a temperature above 300 °C may lead to further ductilization. However, the mechanical strength will be further decreased due to the coarsened microstructure [10]. Similarly, performing multi-pass FSP is expected to homogenize the Si particle distribution which can bring beneficial effects on ductility [27]. However, it is found in our preliminary investigations that repeated thermal input from multiple passes drives the Si particles to grow to larger size, which leads to a decrease in mechanical strength.

6. Conclusions

In this work, the damage mechanism has been investigated in SLM AlSi10Mg under as built and three different post-treatment conditions. The following conclusions can be drawn:

1. The Si-rich network is mainly interconnected in the as built state

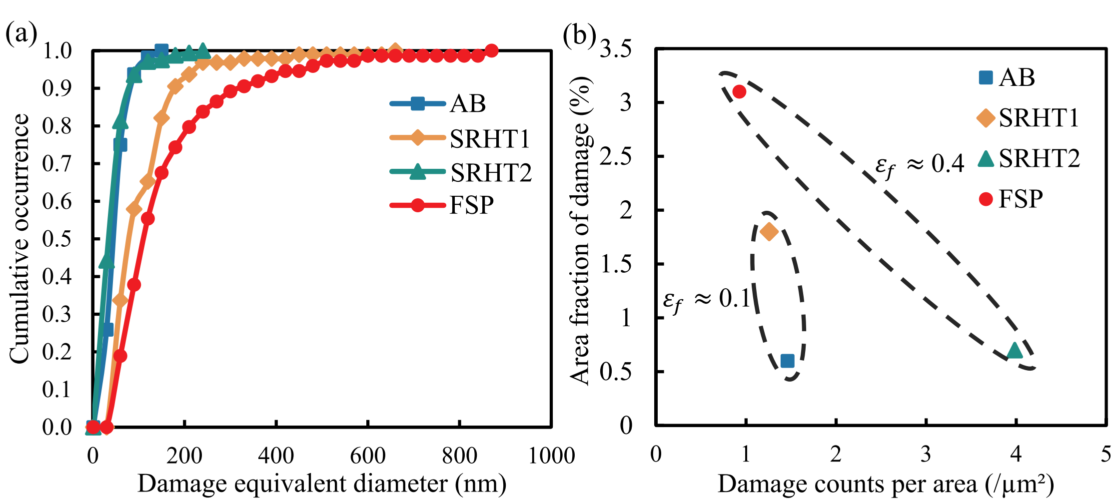

Fig. 15. Statistics of damage size (a) and density (b) in the investigated microstructures.

and this imparts the high mechanical strength. Post-treatments generally globularize the network and lead to strength loss.
2. When the Si-rich network is mostly interconnected, damage occurs at low strain level and the Al cells cannot allow stable void growth since they are subjected to high stress transferred from the Si network.
3. Globularization of the Si phase is necessary for ductility enhancement. A fourfold increase has been achieved accompanied by a strength decrease of roughly 30% via both heat treatment and friction stir processing in the present work. A low porosity (0.09%) has negligible impact on ductility.
4. The increase in ductility can be reached either by relatively early damage nucleation and slow growth and coalescence or by relatively late damage nucleation but fast coalescence.

Data availability

The raw/processed data required to reproduce these findings cannot be shared at this time as the data also forms part of an ongoing study.

Acknowledgments

This research work has been supported by the WALInnov LongLifeAM project, Convention n° 1810016, funded by Service public de Wallonie Économie Emploi Recherche (SPW-EER). L. Ding and A. Simar acknowledge the financial support of the European Research Council (ERC) for the Starting Grant ALUFIX project (grant agreement n° 716678). J. G. Santos Macías acknowledges the support of the Fonds de la recherche scientifique - FNRS (FRIA grant), Belgium. H. Idrissi is mandated by the Belgian National Fund for Scientific Research (FSR-FNRS). Any-Shape is acknowledged for material supply. We thank Prof. P. J. Jacques from UCLouvain for fruitful discussion and critical reading of the paper.

Appendix A. Supplementary data

Supplementary data to this article can be found online at https://doi.org/10.1016/j.msea.2019.138210.

References

[1] E. Uhlmann, R. Kersting, T.B. Klein, M.F. Cruz, A.V. Borille, Additive manufacturing of titanium alloy for aircraft components, Proc. CIRP 35 (2015) 55–60.
[2] I. Yadroitsev, P. Krakhmalev, I. Yadroitsava, Selective laser melting of Ti6Al4V alloy for biomedical applications: temperature monitoring and microstructural evolution, J. Alloy. Comp. 583 (2014) 404–409.
[3] E.O. Olakanmi, R.F. Cochrane, K.W. Dalgarno, A review on selective laser sintering/melting (SLS/SLM) of aluminium alloy powders: processing, microstructure, and properties, Prog. Mater. Sci. 74 (2015) 401–477.
[4] L. Thijs, K. Kempen, J.P. Kruth, J.V. Humbeeck, Fine-structured aluminium products with controllable texture by selective laser melting of pre-alloyed AlSi10Mg powder, Acta Mater. 61 (2013) 1809–1819.
[5] N.O. Larrosa, W. Wang, N. Read, M.H. Loretto, C. Evans, J. Carr, U. Tradowsky, Linking microstructure and processing defects to mechanical properties of selectively laser melted AlSi10Mg alloy, Theor. Appl. Fract. Mech. 98 (2018) 123–133.
[6] P. Delroisse, P.J. Jacques, E. Maire, O. Rigo, A. Simar, Effect of strut orientation on the microstructure heterogeneities in AlSi10Mg lattices processed by selective laser melting, Scr. Mater. 141 (2017) 32–35.
[7] Z.H. Xiong, S.L. Liu, S.F. Li, Y. Shi, Y.F. Yang, R.D.K. Misra, Role of melt pool boundary condition in determining the mechanical properties of selective laser melting AlSi10Mg alloy, Mater. Sci. Eng. A 740–741 (2019) 148–156.
[8] T.M. Mower, M.J. Long, Mechanical behavior of additive manufactured, powder-bedlaser-fused materials, Mater. Sci. Eng. A 651 (2016) 198–213.
[9] B. Chen, S.K. Moon, X. Yao, G. Bi, J. Shen, J. Umeda, K. Kondoh, Strength and strain hardening of a selective laser melted AlSi10Mg alloy, Scr. Mater. 141 (2017) 45–49.
[10] N. Takata, H. Kodaira, K. Sekizawa, A. Suzuki, M. Kobashi, Change in microstructure of selectively laser melted AlSi10Mg alloy with heat treatments, Mater. Sci. Eng. A 704 (2017) 218–228.
[11] E. Brandl, U. Heckenberger, V. Holzinger, D. Buchbinder, Additive manufactured AlSi10Mg samples using Selective Laser Melting (SLM): microstructure, high cycle fatigue, and fracture behavior, Mater. Des. 34 (2012) 159–169.
[12] L. Zhou, A. Mehta, E. Schulz, B. McWilliams, K. Cho, Y. Sohn, Microstructure, precipitates and hardness of selectively laser melted AlSi10Mg alloy before and after heat treatment, Mater. Char. 143 (2018) 5–17.
[13] N.E. Uzan, R. Shneck, O. Teheskel, N. Frage, Fatigue of AlSi10Mg specimens fabricated by additive manufacturing selective laser melting (AM-SLM), Mater. Sci. Eng. A 704 (2017) 229–237.
[14] I. Rosenthal, R. Shneck, A. Stern, Heat treatment effect on the mechanical properties and fracture mechanism in AlSi10Mg fabricated by additive manufacturing selective laser melting, Mater. Sci. Eng. A 729 (2018) 310–322.
[15] A.H. Maamoun, S.C. Veldhuis, M. Elbestawi, Friction stir processing of AlSi10Mg parts produced by selective laser melting, J. Mater. Process. Technol. 263 (2019) 308–320.
[16] J.G. Santos Macías, C. Elangeswaran, L. Zhao, B. Van Hooreweder, J. Adrien, E. Maire, J.Y. Buffière, W. Ludwig, P.J. Jacques, A. Simar, Ductilisation and fatigue life enhancement of selective laser melted AlSi10Mg by friction stir processing, Scr. Mater. 170 (2019) 124–128.
[17] T. Yang, K. Wang, W. Wang, P. Peng, L. Huang, K. Qiao, Y. Jin, Effect of friction stir processing on microstructure and mechanical properties of AlSi10Mg aluminum alloy produced by selective laser melting, J. Occup. Med. 71 (2019) 1–11.
[18] X. Yan, S. Yin, C. Chen, C. Huang, R. Bolot, R. Lupoi, M. Kuang, W. Ma, C. Coddet, H. Liao, M. Liu, Effect of heat treatment on the phase transformation and mechanical properties of Ti6Al4V fabricated by selective laser melting, J. Alloy. Comp. 764 (2018) 1056–1071.
[19] C. Huang, X. Yan, L. Zhao, M. Liu, W. Ma, W. Wang, J. Soete, A. Simar, Ductilization of selective laser melted Ti6Al4V alloy by friction stir processing, Mater. Sci. Eng. A 755 (2019) 85–96.
[20] D. Kim, W. Woo, J. Hwang, K. An, S. Choi, Stress partitioning behavior of an AlSi10Mg alloy produced by selective laser melting during tensile deformation using in situ neutron diffraction, J. Alloy. Comp. 686 (2016) 281–286.
[21] D. Kim, J. Hwang, E. Kim, Y. Heo, W. Woo, S. Choi, Evaluation of the stress-strain relationship of constituent phases in AlSi10Mg alloy produced by selective laser melting using crystal plasticity FEM, J. Alloy. Comp. 714 (2016) 687–697.
[22] M.W. Hyer, Stress Analysis of Fiber-Reinforced Composite Materials, DEStech Publications, Inc., 2009.
[23] J. Wu, X.Q. Wang, M.M. Attallah, M.H. Loretto, Microstructure and strength of selectively laser melted AlSi10Mg, Acta Mater. 117 (2016) 311–320.
[24] N. Takata, H. Kodaira, A. Suzuki, M. Kobashi, Size dependence of microstructure of AlSi10Mg alloy fabricated by selective laser melting, Mater. Char. 143 (2018) 18–26.
[25] D. Lassance, D. Fabrègue, F. Delannay, T. Pardoen, Micromechanics of room and high temperature fracture in 6xxx Al alloys, Prog. Mater. Sci. 52 (2007) 62–129.
[26] F. Hannard, T. Pardoen, E. Maire, C.L. Bourlot, R. Mokso, A. Simar, Characterization and micromechanical modelling of microstructural heterogeneity effects on ductile fracture of 6xxx aluminium alloys, Acta Mater. 103 (2016) 558–572.
[27] F. Hannard, S. Castin, E. Maire, R. Mokso, T. Pardoen, A. Simar, Ductilization of aluminium alloy 6056 by friction stir processing, Acta Mater. 130 (2017) 121–136.
[28] R.S. Mishra, Z.Y. Ma, Friction stir welding and processing, Mater. Sci. Eng. R 50 (2005) 1–78.
[29] Z.Y. Ma, Friction stir processing technology: a review, Metall. Mater. Trans. A 39 (2008) 642–658.
[30] C. Jonckheere, B. de Meester, A. Denquin, A. Simar, Torque, temperature and hardening precipitation evolution in dissimilar friction stir welds between 6061-T6 and 2014-T6 aluminium alloys, J. Mater. Process. Technol. 213 (2013) 826–837.
[31] ABAQUS/Standard User's Manual, Providence, RI, (2016).
[32] V.C. Nardone, K.M. Prewo, On the strength of discontinuous silicon carbide reinforced aluminium composites, Scr. Metall. 20 (1986) 43–48.
[33] A. Pineau, A.A. Benzerga, T. Pardoen, Failure of metals I: brittle and ductile fracture, Acta Mater. 107 (2016) 424–483.
[34] T.B. Cox, J.R. Low, An investigation of the plastic fracture of AISI 4340 and 18 Nickel-200 grade maraging steels, Metall. Mater. Trans. B 5 (1974) 1457–1470.
[35] L. Babout, E. Maire, R. Fougères, Damage initiation in model metallic materials: X-ray tomography and modelling, Acta Mater. 52 (2004) 2475–2487.
[36] A. E. Wilson-Heid, T. C. Novak, A. M.Beese, Characterization of the effects of internal pores on tensile properties of additively manufactured austenitic stainless steel 316L, Exp. Mech, https://doi.org/10.1007/s11340-018-00465-0.